3D LiDAR Aided GNSS NLOS Mitigation for Reliable GNSS-RTK Positioning in Urban Canyons

Xikun Liu, Weisong Wen, Feng Huang, Han Gao, Yongliang Wang, Li-Ta Hsu

***Abstract*—GNSS real-time kinematic (RTK) and LiDAR odometry are complementary, offering global and local positioning capabilities, respectively. GNSS-RTK/LiDAR integration primarily focuses on two aspects: (1) 3D LiDAR-aided (3DLA) GNSS non-line-of-sight (NLOS) mitigation using point cloud data. (2) State estimation via tightly-coupled GNSS/LiDAR integration, which improves GNSS geometry, yielding better float solutions and lower estimation uncertainty. Combining 3DLA NLOS mitigation with tightly-coupled integration can thus enhance urban positioning reliability. However, the current 3DLA GNSS-RTK system remains limited in terms of NLOS detection reliability, tightly-coupled integration effectiveness, and computational efficiency. This paper proposes a tightly-coupled GNSS-RTK/LiDAR/INS integration system with 3DLA NLOS mitigation. We focus on improving the robustness of 3DLA NLOS detection, the efficiency and effectiveness of the tightly-coupled GNSS-RTK/LiDAR integration. Evaluations on the challenging UrbanNav dataset show over 70% improvement in positioning accuracy compared to conventional GNSS-RTK, achieving sub-meter to meter-level precision. Runtime analysis confirms the system supports real-time optimization and ambiguity resolution with an average computation time of 70 ms.**

***Index Terms*—GNSS-RTK, LiDAR-aided GNSS, NLOS exclusion, Geometry distribution, Urban canyons.**

I. INTRODUCTION

THE global navigation satellite system (GNSS) provides high-precision positioning and plays a key role in modern autonomous navigation. GNSS real-time kinematic (RTK) [1] achieves centimeter-level accuracy using reference station corrections in open-sky areas. It first estimates the float solution using double-differenced (DD) [2] pseudorange and carrier-phase measurements, and then resolves integer ambiguities via integer least-squares (e.g LAMBDA and its variants [3, 4]). However, GNSS-RTK performance degrades significantly in urban canyons due to signal blockage and reflection (Fig. 1). There are two main factors leading to the impact. First, many GNSS signals in urban areas are non-line-of-sight (NLOS) [5], caused by reflections from buildings [6] or dynamic objects (e.g., double-decker buses) [7]. Such polluted measurements can significantly degrade the accuracy of the float solution. Second, buildings and moving objects block many satellite signals, limiting the number of received satellites. In other words, only satellites with high elevation angles are received. This leads to poor geometry [8], reducing the success rate of ambiguity resolution (AR) and positioning accuracy.

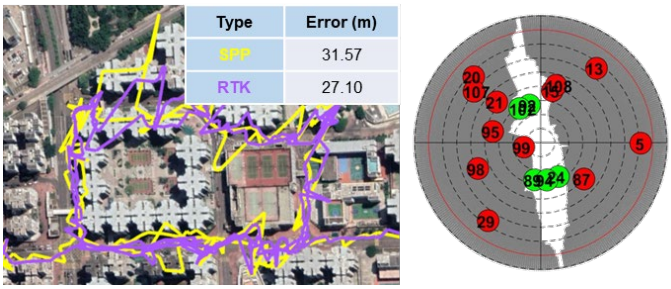

Fig. 1. Illustration of the challenges faced by GNSS-RTK in an urban canyon. The left figure shows the comparison of trajectory and error in meters between SPP and GNSS-RTK positioning methods based on low-cost receivers. The right figure shows the skyplot of a randomly selected location where the red and green dots denote the NLOS and LOS signals, respectively. The numbers indicate pseudorandom noise (PRN), which is used to distinguish different satellites.

With the growing availability of onboard sensors, multi-sensor integration has been widely explored in recent decades. Recent research on inertial measurement unit (IMU), visual sensors, Light detection and ranging (LiDAR) sensors, and their integration for positioning systems has demonstrated impressive local positioning and perception capabilities [9-11]. Integrating these sensors with GNSS offers a promising solution to the above challenges, improving positioning accuracy in complex environments like urban canyons.

One approach to the first challenge is leveraging other sensors' relative positioning to predict and validate GNSS observations [12-15]. These methods require high local positioning accuracy and reliable initial states. Since NLOS signals result from reflections off surrounding structures, some studies use sensors with broad environmental perception (e.g., camera or LiDAR) or pre-built maps for NLOS detection [16, 17]. Visual-based approaches [18, 19] utilize a sky-pointing fish-eye camera with segmentation algorithms to classify visible and blocked sky regions. Satellite visibility is then used for NLOS detection and exclusion. Leveraging LiDAR's wide perception range and accuracy, our previous work proposed 3D LiDAR-aided (3DLA) GNSS single point positioning (SPP) and GNSS-RTK methods that reconstruct the

This work was supported in part by the __ under Grant __. *Corresponding author: Weisong Wen.*

Xikun Liu, Weisong Wen, and Li-Ta Hsu are all with Hong Kong Polytechnic University, Hong Kong. (e-mail: xi-kun.liu@connect.polyu.hk, welson.wen@polyu.edu.hk, lt.hsu@polyu.edu.hk)

Han Gao and Yongliang Wang are with Huawei Technologies (e-mail: gaohan14@huawei.com, wangyongliang775@huawei.com).

environment using a point cloud map (PCM) to exclude [7, 20, 21] or even correct [6, 22] NLOS receptions. To initialize PCM for NLOS detection, existing method [23] uses external Attitude and Heading Reference System (AHRS) devices to obtain orientation information. However, such systems require magnetometers. An alternative approach estimates orientation from Doppler observations [24], but the Doppler-based heading estimation tends to be highly inaccurate in dense urban areas. These issues can degrade the accuracy of the PCM pose used for NLOS detection, ultimately affecting the reliability of the detection results.

Besides unhealthy measurements, poor satellite geometry also limits GNSS-RTK performance in urban canyons. In particular, poor satellite geometry provides weak constraints on the estimated states. Recent work has aimed to improve geometry via tightly-coupled fusion, the integration of GNSS/INS [25, 26], GNSS/INS/vision [27-29], and GNSS/INS/LiDAR [30-36] have shown impressive results on improving positioning availability and accuracy. In tightly coupled GNSS/LiDAR systems, LiDAR constraints can be categorized into two types. The first type involves relative constraints [30, 33, 35], such as scan-to-scan matching, where LiDAR observations help local relative pose refinement under the assumption that GNSS provides globally accurate position estimates. However, if GNSS suffers from large errors, the system may fail to estimate the correct trajectory. The second type uses LiDAR to provide absolute constraints by matching scans to a local map [31, 32, 36]. When the local map is accurate, LiDAR can still provide reliable position estimates even when GNSS observations are degraded. On the other hand, if the map is inaccurate, LiDAR constraints may negatively affect positioning accuracy. This work focuses on the second type of constraint. However, two challenges remain underexplored in current research. First, using a large number of LiDAR observations can pose computational challenges, especially for real-time applications. Few existing works investigate the use of reduced LiDAR features in tightly coupled fusion systems. It remains unclear how a smaller number of LiDAR features affects the system's ability to constrain the state, particularly in complex urban environments. Inspired by prior studies on feature degradation in LiDAR SLAM [37], there is a need to analyze the relationship between the number of LiDAR observations and their constraint effectiveness. Furthermore, since both scan-to-map LiDAR constraints and GNSS pseudorange/career measurements provide absolute positioning information at a comparable accuracy level, an overabundance of LiDAR features may dominate the optimization. Therefore, balancing the weights of LiDAR and GNSS observations is critical to ensure robust and accurate positioning in tightly coupled systems.

In this work, we extend the existing 3D LiDAR aided (3DLA) GNSS-RTK framework in two key directions. First, we aim to enhance the robustness of 3DLA-based NLOS exclusion by investigating more reliable PCM construction and update strategies through GNSS/LiDAR integration. Second, we explore a more efficient tightly coupled GNSS/LiDAR fusion approach to improve the geometric distribution of satellite observations. Particular attention is given to balancing the contributions of different sensor modalities in the state estimation process. In the proposed system, NLOS receptions are first detected and excluded through the incrementally generated and drift-free sliding window-based PCM. Sparse LiDAR landmarks are used to generate virtual satellites (VS), which improve GNSS geometry by tightly integrating raw measurements from GNSS, VS, and IMU. After optimization, AR is performed based on the float solution and covariance improved by the VS. Meanwhile, the improved float and fixed solutions are further employed to correct PCM drift, ensuring reliable NLOS detection. The main contributions of the proposed work are listed as follows:

1. *Tackle the first challenge of GNSS-RTK by GNSS NLOS mitigation*: In this paper, we propose a drift-free 3D sliding window PCM-based GNSS NLOS mitigation method to improve the quality of the raw GNSS measurements. The PCM drift is corrected by pose graph optimization (PGO) after integration.
2. *Tackle the second challenge of GNSS-RTK by geometry distribution improvement using VS*: In this paper, we tightly fuse the scan-to-map LiDAR constraints, IMU constraints, and GNSS constraints in a sliding window factor graph. In particular, we additionally focus on using fewer LiDAR observations for efficiency and balancing weighting between LiDAR and GNSS measurements.
3. *Extensive evaluation in urban canyons of Hong Kong*: Experiments have been conducted on three challenging urbanized sequences collected in Hong Kong and comprehensive comparisons are carefully conducted to show the effectiveness of the proposed method.

The rest of the paper is organized as follows: The proposed 3D LiDAR-aided GNSS-RTK method with the detailed measurements model and residuals formulation are given in Section II. Section III elaborates on the experiments and evaluation results of the proposed method. Conclusion and potential further development are given in Section IV.

II. METHODOLOGY

A. System Overview

The pipeline of the proposed system is depicted in Fig. 2. The system consists of two major parts, namely 3D LiDAR-aided NLOS exclusion, and integrated positioning with VS-aided geometry improvement. The system inputs include raw GNSS (pseudorange, carrier phase, and Doppler), LiDAR, and IMU measurements. All measurements are processed under a common keyframe mode [11] to balance computation and redundancy. The raw IMU data are preprocessed using the pre-integration technique [38]. The initial pose of each new keyframe is propagated using IMU data. The keyframe poses and the corresponding 3D PCM are used to detect NLOS and cycle slips [39]. VS constraints are generated using the extracted features and PCM [40]. After preprocessing, the

TABLE I
NOTATIONS

Notation	Description	Notation	Description
$(\cdot)_t$	GNSS epoch	$\dot{\delta}$	Clock bias drift
$(\cdot)^s$	Satellite index	c	Speed of light
$(\cdot)^w$	Master satellite index	r	Residual
$(\cdot)_r$	Receiver	r	Range
$(\cdot)_e$	Reference station	**e**	Unit vector
λ	Wavelength	**v**	Velocity
d	Doppler measurement	**p**	Position
ρ	Pseudorange measurement	$\boldsymbol{l}$	Transmission vector

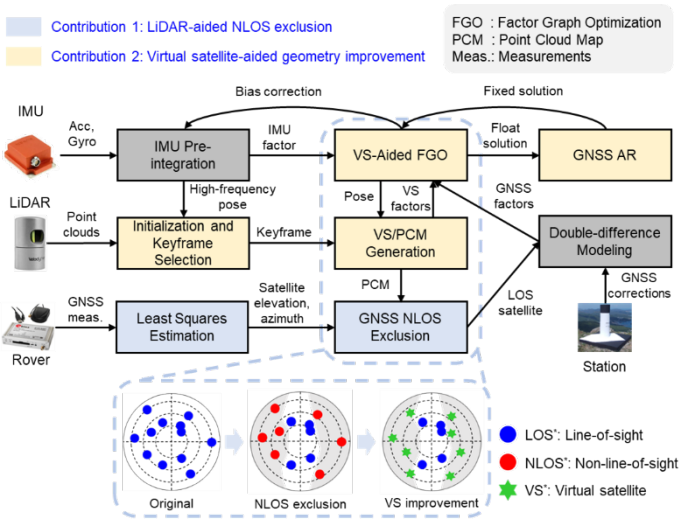

Fig. 2. Pipeline overview of the proposed system.

sliding window states are jointly optimized via factor graph optimization (FGO) using constraints from VS, GNSS, and IMU. This yields an improved float solution with position and covariance. The optimized position and covariance are then used for AR to obtain a fixed solution. Global pose graph optimization is then performed using both fixed and float solutions. The updated poses and PCM support the next GNSS NLOS detection iteration. To ensure real-time performance, a marginalization strategy is used to discard old measurements [11]. The methodology is detailed below. Table I lists key notations for clarity.

B. 3D LiDAR-Aided GNSS NLOS Mitigation

NLOS detection and exclusion are first applied to incoming GNSS measurements. We use a fast-search method from our previous work [8] to classify the satellite visibilities based on the local 3D PCM. The 3D PCM is built from recent keyframe point clouds. Compared to our earlier method, our approach reduces PCM attitude drift using GNSS-RTK corrections through PGO. While PCM-based visibility classification is not novel, we briefly outline the key steps for completeness.

Our method contains three steps: (1) Maintaining a sliding-window PCM built from the last n_{NL} keyframes. n_{NL} is set to cover a PCM range of up to 250m, as NLOS is typically caused by nearby objects [6]. (2) A fixed-step search along the line-of-sight (LOS) direction is used to classify satellite visibility (Fig. 3a). The LOS vector is calculated from the receiver and satellite positions. The search starts at the receiver's position $\mathbf{p}_{r,t}^{EN}$ and moves in Δd steps along the LOS. At each step, we count neighboring PCM points within radius Δr. The values of step size Δd and search radius Δr are chosen based on the resolution of the 3D PCM. To avoid missing intersections with objects (i.e., tunneling through reflection surfaces), the radius Δr is set larger than the PCM resolution. We also make sure that Δd and Δr are set so that neighboring search regions overlap, which helps detect small structures. In our setup, we use Δd = 0.4m and Δr = 0.8m. If the neighboring number is larger than the threshold, then the satellite will be classified as invisible, and the relevant measurement is excluded as NLOS receptions. The threshold is conservatively set to 3 based on Δr and minimum point spacing in PCM. The threshold is to prevent NLOS detection being triggered by noisy point returns. However, drift during driving introduces attitude errors that bias the PCM and impair NLOS classification. In other words, the 3D PCM-aided NLOS detection relies heavily

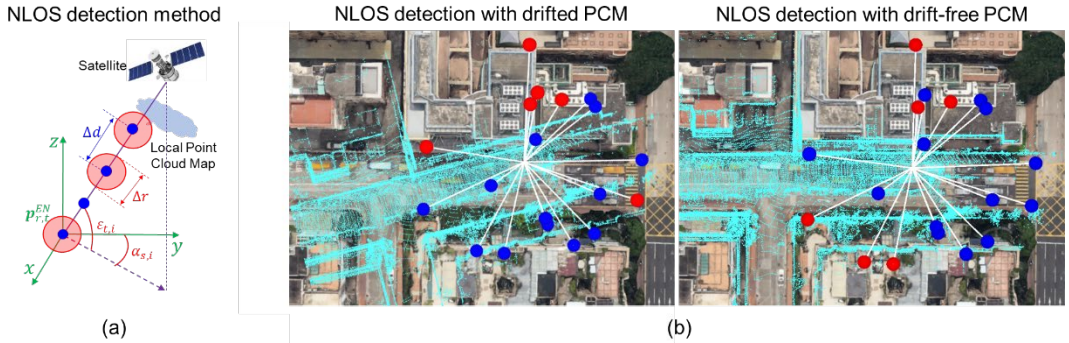

Fig. 3. Illustration of the proposed 3D LiDAR-aided NLOS detection based on drift-free PCM. (a) shows the details of the detection method. (b) shows the comparison of satellites' occlusion in the same epoch by drifted- and drifted-free-PCM. The red dots are detected NLOS satellites, while the blue dots represent the LOS satellites. The detection result and the PCM are projected on *Google Earth*.

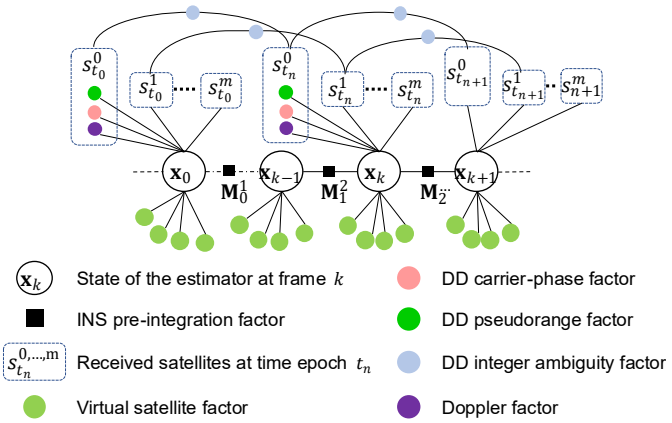

Fig. 4. The factor graph of the proposed tightly-coupled integration system.

on accurate attitude estimation, which is easily affected by the drift. Fig. 3b illustrates how the drifted PCM will affect the detection result. To address this, we apply global pose graph optimization to correct drift and improve NLOS detection. The global optimization is based on the improved GNSS-RTK positioning results introduced in the following sections. Fig. 3b also shows the illustration of the proposed drift-free PCM-based NLOS exclusion. It is observed that, before LiDAR-aided NLOS exclusion, nearly one-third of the satellites blocked by buildings and trees were originally used as LOS satellites, which causes large positioning errors. On the other hand, the drift-free PCM provides the correct environmental information, which leads to accurate NLOS detection.

C. VS aided GNSS-RTK/IMU Factor Graph Optimization and Ambiguity Resolution

This section presents the tightly-coupled VS-aided GNSS-RTK/IMU FGO and AR method. System states are initialized in the ENU frame using sensor extrinsic. The body frame is defined at the IMU center. The system states include:

1. The position $\mathbf{p}_{b,k}^{EN}$ and orientation $\mathbf{q}_{b,k}^{EN}$ of the IMU in ENU coordinates. k represents the kth keyframe in the sliding window.
2. The velocity $\mathbf{v}_{b,k}^{EN}$ of the IMU in ENU coordinate. $\mathbf{b}_a$ and $\mathbf{b}_w$ represent the bias of the gyroscope and accelerometer, respectively.
3. The DD integer ambiguities $N_{DD,r,t}^{S}$ of all received satellites $s \in S$ to receiver r at time epoch t.
4. The clock drift $\dot{\delta}_{r,t}$ of receiver r at time epoch t.

The system states within the sliding window can be further expressed as:

$$\begin{aligned} \boldsymbol{\chi} &= \left[x_0, \cdots, x_{K-1}, N_{DD,r,t_0}^{S}, \cdots, N_{DD,r,t_{n-1}}^{S}, \dot{\delta}_{t_0}^{r}, \cdots, \dot{\delta}_{t_{n-1}}^{r}\right] \\ With\, x_k &= \left[\mathbf{p}_{b,k}^{EN},\ \mathbf{q}_{b,k}^{EN}, \mathbf{v}_{b,k}^{EN},\ \mathbf{b}_a,\ \mathbf{b}_w\right] \\ N_{DD,r,t}^{S} &= \left[N_{DD,r,t}^{s_0}, \cdots, N_{DD,r,t}^{s_{m-1}}\right] \end{aligned} \tag{1}$$

where $k \in [0, \cdots, K-1]$, K represents the size of the sliding window, $t \in [t_0, \cdots, t_{n-1}]$ represents the received epoch of the GNSS signal, n represents the epoch number of the received GNSS measurements within the time interval of the sliding window, and m denotes the number of received satellites at time epoch t.

The optimal state estimation is achieved by maximizing the posterior probability given the measurements. The measurements are assumed to be independent and with zero-mean Gaussian-distributed noise. The problem is formulated as the following objective function:

$$\begin{aligned} \boldsymbol{\chi}^* = \underset{\boldsymbol{\chi}}{\operatorname{argmin}} \sum_{S,r,k,t} \Big(&\left\|\mathbf{r}_p - \mathbf{H}_p\boldsymbol{\chi}\right\| + \left\|\mathbf{r}_{L,k}\right\|_{\boldsymbol{\Sigma}_L}^2 + \left\|\mathbf{r}_{B,k}\right\|_{\boldsymbol{\Sigma}_B}^2 + \\ &\left\|\mathbf{r}_{DD,\rho,r,t}^{S}\right\|_{\sigma_\rho}^2 + \left\|\mathbf{r}_{DD,\psi,r,t}^{S}\right\|_{\sigma_\psi}^2 + \left\|\mathbf{r}_{DD,N,r,t}^{S}\right\|_{\sigma_N}^2 + \left\|\mathbf{r}_{d,r,t}^{S}\right\|_{\sigma_d}^2 \Big) \end{aligned} \tag{2}$$

where $\{\mathbf{r}_p, \mathbf{H}_p\}$ denotes the marginalized term as prior constraints. $\mathbf{r}_{B,k}$ represents the IMU factor, which is weighted by the relative covariance matrix $\boldsymbol{\Sigma}_B$. $\boldsymbol{\Sigma}_B$ is estimated based on the inverse of the measurement noise covariance which is linearly propagated based on the given measurement white noise and the bias random walk within the integration interval [38]. $\mathbf{r}_{L,k}$ represents the VS factor and is weighted by the covariance matrix $\boldsymbol{\Sigma}_L$. The estimation of $\boldsymbol{\Sigma}_L$ will be introduced in the following section. $\mathbf{r}_{DD,\rho,r,t}^{S}$, $\mathbf{r}_{DD,\psi,r,t}^{S}$ and $\mathbf{r}_{d,r,t}^{S}$ denote the DD GNSS pseudorange, carrier phase, and Doppler factors, respectively. The uncertainties of different observations are given as $\sigma_\psi = \frac{\sigma_\rho}{100}$ and $\sigma_d = \sigma_\rho$, where the σ_ρ is initialized by SNR and elevation angle following the method in *goGPS* software [41], the parameters are $A = 30$, $s0 = 10$, $s1 = 50$, $a = 30$. $\mathbf{r}_{DD,N,r,t}^{S}$ denotes the constant integer ambiguity factor weighted by $\sigma_N = \sigma_\psi$.

The factor graph structure of the proposed system is shown in Fig. 4. The VS factors and IMU factors directly constrain the system states x_k. Due to the lower frequency of GNSS data, the GNSS factors (DD pseudorange, DD carrier phase, and Doppler factors) constrain the system states x_k and x_{k+1} via an interpolated states x_t at time epoch t, where $t \in (k, k+1)$.

1. GNSS DD Pseudorange/Carrier Phase Factor

The pseudorange measurement $\rho_{r,t}^{s}$ of the GNSS receiver r at time t is expressed by:

$$\rho_{r,t}^{s} = \mathrm{r}_{r,t}^{s} + c\left(\delta_{r,t} - \delta_{s,t}\right) + I_{r,t}^{s} + T_{r,t}^{s} + \varepsilon_{\rho,r,t}^{s} \tag{3}$$

where $r_{r,t}^{s}$ denotes the geometric range between satellite s and receiver r at time epoch t. $I_{r,t}^{s}$ represents the ionospheric delay distance, $T_{r,t}^{s}$ represents the tropospheric delay distance. $\varepsilon_{\rho,r,t}^{s}$ denotes the other errors including multipath error, NLOS error, receiver noise error, and antenna phase-related noise error.

Similar to the pseudorange, the carrier phase measurements of the GNSS receiver r at time t can be expressed as:

$$\begin{aligned} \lambda\psi_{r,t}^{s} = \mathrm{r}_{r,t}^{s} + c\left(\delta_{r,t} - \delta_{s,t}\right) - I_{r,t}^{s} + T_{r,t}^{s} \\ + \lambda B_{r,t}^{s} + d\psi_{r,t}^{s} + \varepsilon_{\psi,r,t}^{s} \end{aligned} \tag{4}$$

where $B_{r,t}^{s} = \psi_{r,t,0} - \psi_{0,r,t}^{s} + N_{r,t}^{s}$ represents the carrier phase bias. The variable $\psi_{r,t,0}$ denotes the initial phase of the receiver's

local oscillator. $\psi^s_{0,r,t}$ is the initial phase of the transmitted navigation signal from the satellite. The variable $N^s_{r,t}$ is the carrier phase integer ambiguity which should be an integer value. λ denotes the carrier wavelength of the respective satellite system. $d\psi^s_{r,t}$ represents the carrier phase correction terms, which contain antenna phase offsets and variations, station displacement by earth tides, phase windup effects, and a relativity correction on the satellite clock. $\varepsilon^s_{\psi,r,t}$ represents errors caused by multipath effects, NLOS receptions, receiver noise, and antenna delay.

Clock and atmospheric errors significantly affect positioning accuracy. Therefore, the DD technique is applied in GNSS-RTK. It first computes a single difference between the measurements from the rover *r* and reference station *e* to the same satellite, then subtracts the single differences of two satellites to form a double difference. The master satellite w is selected as the one with the highest elevation, as it is less prone to multipath and NLOS errors. At each epoch, all other satellites share the same master satellite for a given system. The DD pseudorange and carrier phase are formulated as follows:

$$\rho^s_{DD,r,t} = \left(\rho^s_{r,t} - \rho^s_{e,t}\right) - \left(\rho^w_{r,t} - \rho^w_{e,t}\right) \quad (5)$$

$$\psi^s_{DD,r,t} = \left(\psi^s_{r,t} - \psi^s_{e,t}\right) - \left(\psi^w_{r,t} - \psi^w_{e,t}\right) \quad (6)$$

Considering that the receiver *r* and reference station *e* are under similar atmospheric conditions, the single difference operation can eliminate atmospheric errors and satellite clock bias. The second difference operation removes the receiver clock bias. Therefore, the DD pseudorange and DD carrier phase measurements model are given as:

$$\rho^s_{DD,r,t} = \left(\mathrm{r}^s_{r,t} - \mathrm{r}^s_{e,t}\right) - \left(\mathrm{r}^w_{r,t} - \mathrm{r}^w_{e,t}\right) + \varepsilon^s_{DD,\rho,r,t} \quad (7)$$

$$\lambda\psi^s_{DD,r,t} = \left(\mathrm{r}^s_{r,t} - \mathrm{r}^s_{e,t}\right) - \left(\mathrm{r}^w_{r,t} - \mathrm{r}^w_{e,t}\right) + N^s_{DD,r,t} + \varepsilon^s_{DD,\psi,r,t} \quad (8)$$

where $\varepsilon^s_{DD,\rho,r,t}$, $\varepsilon^s_{DD,\psi,r,t}$ represents the noise of DD pseudorange measurements and carrier phase measurements. $N^s_{DD,r,t}$ is the DD integer ambiguity of satellite s, which is one of the system states to be estimated.

Given the DD measurement model above, the DD pseudorange residuals and DD carrier phase residuals are formed as:

$$r^s_{DD,\rho,r,t} = \rho^s_{DD,r,t} - \left(\mathrm{r}^s_{r,t} - r^s_{e,t}\right) - \left(\mathrm{r}^w_{r,t} - \mathrm{r}^w_{e,t}\right) \quad (9)$$

$$r^s_{DD,\psi,r,t} = \lambda_i\psi^s_{DD,r,t} - \left(\mathrm{r}^s_{r,t} - \mathrm{r}^s_{e,t}\right) - \left(\mathrm{r}^w_{r,t} - \mathrm{r}^w_{e,t}\right) - N^s_{DD,r,t} \quad (10)$$

where the range distances $\mathrm{r}^s_{r,t}$, $\mathrm{r}^s_{e,t}$, $\mathrm{r}^w_{r,t}$ and $\mathrm{r}^w_{e,t}$ are calculated based on the positions of the GNSS receiver:

$$\mathrm{r}^s_{r,t} = \left\|\mathbf{p}^{EC}_{r,t} - \mathbf{p}^{EC}_{s,t}\right\|, \mathrm{r}^s_{e,t} = \left\|\mathbf{p}^{EC}_{e} - \mathbf{p}^{EC}_{s,t}\right\|,$$
$$\mathrm{r}^w_{r,t} = \left\|\mathbf{p}^{EC}_{r,t} - \mathbf{p}^{EC}_{w,t}\right\|, \mathrm{r}^w_{e,t} = \left\|\mathbf{p}^{EC}_{e} - \mathbf{p}^{EC}_{w,t}\right\| \quad (11)$$

where $\|*\|$ denotes the norm of the vector. $\mathbf{p}^{EC}_{s,t}$ and $\mathbf{p}^{EC}_{w,t}$ are satellite positions transformed in the ECEF frame, $\mathbf{p}^{EC}_{e}$ is the position of the reference station in the ECEF frame. The estimated $\mathbf{p}^{EC}_{r,t}$ is the position of the GNSS receiver r at time epoch t in the ECEF frame transformed from $\mathbf{p}^{EN}_{r,t}$. Notably, the transformation from ENU to ECEF according to the origin point $\mathbf{p}^{EC}_{o}$ is calculated as:

$$\mathbf{p}^{EC}_{r,t} = \mathbf{R}^{EC}_{EN}\mathbf{p}^{EN}_{r,t} + \mathbf{p}^{EC}_{o} \quad (12)$$

$$\mathbf{R}^{EC}_{EN} = \begin{bmatrix} -\sin\lambda_o & -\sin\phi_o\cos\lambda_o & \cos\phi_o\cos\lambda_o \\ \cos\lambda_o & -\sin\phi_o\sin\lambda_o & \cos\phi_o\sin\lambda_o \\ 0 & \cos\phi_o & \sin\phi_o \end{bmatrix} \quad (13)$$

where λ_o and ϕ_o denote the geographic latitude and longitude of the known origin point $\mathbf{p}^{EC}_{o}$.

Further, the receiver's position $\mathbf{p}^{EN}_{r,t}$ is obtained from the estimated states $\mathbf{p}^{EN}_{b,t}$ maintained in the body frame as:

$$\mathbf{p}^{EN}_{r,t} = \mathbf{p}^{EN}_{b,t} + \mathbf{R}^{b}_{r}\mathbf{p}^{b}_{r} \quad (14)$$

In addition, the maintained states are with LiDAR keyframe time t_k rather than GNSS epoch time t. Therefore, linear interpolation is adopted between the system states $\mathbf{p}^{EN}_{b,k}$ and $\mathbf{p}^{EN}_{b,k+1}$ in the adjacent epochs t_k and t_{k+1} with $t \in [t_k, t_{k+1}]$ to obtain the corresponding state $\mathbf{p}^{EN}_{b,t}$, which is calculated based on the ratio of the time interval:

$$\mathbf{p}^{EN}_{b,t} = \left\{\frac{t - t_k}{t_{k+1} - t_k}\mathbf{p}^{EN}_{b,k} + \frac{t_{k+1} - t}{t_{k+1} - t_k}\mathbf{p}^{EN}_{b,k+1}\right\} \quad (15)$$

2. GNSS Constant Integer Ambiguity Factor

GNSS-RTK positioning accuracy suffers if cycle slips are not detected and properly handled. Cycle slip occurs when signal tracking is lost, often due to obstructions like buildings or trees. In such cases, previously resolved integer ambiguities become invalid and must be re-estimated. Without cycle slips, the integer ambiguity remains constant between adjacent epochs. The constant integer ambiguity residual can be formed as:

$$r^s_{DD,N,r,t} = N^s_{DD,r,t} - N^s_{DD,r,t-1} \quad (16)$$

where $N^s_{DD,r,t}$ and $N^s_{DD,r,t-1}$ represent the integer ambiguities of satellite s at time epoch t and epoch $t-1$, respectively.

To eliminate the impact of cycle slips, we adopt a LiDAR-aided detection method [39] based on consistency checks using triple differences formed from two double differences across epochs. Triple difference estimation is performed using state predictions from LiDAR and IMU measurements. According to (8), the DD integer ambiguity for satellite s at time epoch t is estimated as:

$$N^s_{DD,r,t} = \lambda\psi^s_{DD,r,t} - \left(\left(\mathrm{r}^s_{r,t} - \mathrm{r}^s_{e,t}\right) - \left(\mathrm{r}^w_{r,t} - \mathrm{r}^w_{e,t}\right)\right) \quad (17)$$

then the TD integer ambiguity between time epoch t and $t-1$ can be calculated by:

$$N^s_{TD,r,t} = N^s_{DD,r,t} - N^s_{DD,r,t-1} \quad (18)$$

when $N^s_{TD,r,t}$ is larger than a certain threshold $N^{threshold}_{TD}$, the cycle slip occurs at time t. The threshold $N^{threshold}_{TD}$ is set as 3 cycles as described in [39]. According to (17), the TD uses range distance to estimate the DD integer ambiguity, which relies on the high quality of the initial guess of the position. Thanks to LiDAR and IMU, the system can provide a high-quality initial guess, which even enables the detection of small cycle slips.

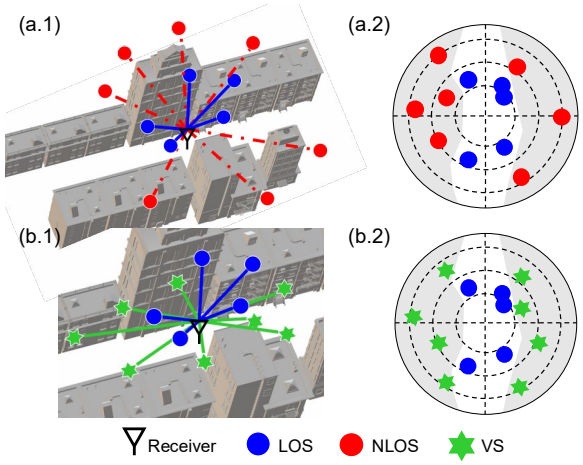

Fig. 5. Illustration of VS-aided GNSS-RTK positioning.

3. GNSS Doppler Factor

Doppler measurement $d_{r,t}^{s}$ at receiver r from satellite s at time epoch t is denoted as:

$$\lambda d_{r,t}^{s} = \mathbf{e}_{r,t}^{s,LOS}\left(\mathbf{v}_{s,t}^{EC} - \mathbf{v}_{r,t}^{EC}\right) + \mathrm{c}\left(\dot{\delta}_{r,t}^{i} - \dot{\delta}_{s,t}\right) + \varsigma_{r,t}^{s} \tag{19}$$

where $\varsigma_{r,t}^{s}$ represents the noise of the received Doppler measurement, c denotes the speed of light. λ denotes the carrier wavelength of the respective satellite constellation system. The velocity of the receiver in the ECEF frame is transformed from the ENU frame using $\mathbf{v}_{r,t}^{EC} = \mathbf{R}_{EN}^{EC}\mathbf{v}_{r,t}^{EN}$. $\mathbf{e}_{r,t}^{s,LOS}$ is the LOS unit vector between the position of receiver r and the satellite s at time epoch t, which is calculated by:

$$\mathbf{e}_{r,t}^{s,LOS} = \left(\frac{\mathbf{p}_{s,t}^{EC} - \mathbf{p}_{r,t}^{EC}}{\left\|\mathbf{p}_{s,t}^{EC} - \mathbf{p}_{r,t}^{EC}\right\|}\right)^{T} \tag{20}$$

Given the Doppler measurement model above, the residual is derived as:

$$r_{d,r,t}^{s} = d_{r,t}^{s} - \frac{1}{\lambda_i}\left(\mathbf{e}_{r,t}^{s,LOS}\left(\mathbf{v}_{s,t}^{EC} - \mathbf{v}_{r,t}^{EC}\right) + \mathrm{c}\left(\dot{\delta}_{r,t}^{i} - \dot{\delta}_{s,t}\right)\right) \tag{21}$$

4. Inertial Factor

The IMU measurements comprise linear acceleration and angular velocity with the effect of corresponding bias and additive noises. Knowing that the frequency of the inertial measurements is practically much higher than other sensors (LiDAR, GNSS), the pre-integration method [38] is further adopted in our optimization to integrate multiple raw inertial measurements into a single relative pose constraint between two consecutive keyframes k and $k+1$. We follow the work from Qin, et al. [11] for the implementation. The readers can refer to [11, 38] for detailed formulation of the inertial factors.

5. LiDAR Landmark-Based VS Factor

The satellite geometry is often poor in urban areas and will be further deteriorated by NLOS exclusion. As shown in Fig. 5a, only high-elevation LOS satellites (blue circles) remain after NLOS exclusion. This leads to high uncertainty in the direction perpendicular to the street, making float solutions more prone to large errors from small observation biases. On the contrary, Fig. 5b shows virtual satellites (VS, green stars) generated from low-lying structures, which complement high-elevation LOS satellites. The state uncertainties from GNSS observations can be effectively bounded by VS.

The formulation of VS constraints follow a similar approach to feature-based LiDAR-SLAM methods [40]. We evaluated edge-based and plane-based LiDAR odometry in urban areas. Planar features achieved better accuracy and robustness. Therefore, we use planar constraints in a scan-to-map scheme in the system. Planar features are extracted for each keyframe by evaluating local point distributions. Plane correspondences are then found via nearest neighbor search and verified using eigenvalue analysis. Given a transformed planar point $\mathbf{p}_{p,k}^{EN}$ in frame k and three corresponding planar points $\mathbf{p}_{p,k,a}^{EN,M}$, $\mathbf{p}_{p,k,b}^{EN,M}$ and $\mathbf{p}_{p,k,c}^{EN,M}$ defining a planar patch in the local feature map M, the point-to-plane residual is calculated as [40]:

$$\boldsymbol{r}_{l,s,k} = \frac{\left\|\left(\mathbf{p}_{p,k}^{EN} - \mathbf{p}_{p,k,a}^{EN,M}\right)\right\|}{\left\|\left(\mathbf{p}_{p,k,a}^{EN,M} - \mathbf{p}_{p,k,b}^{EN,M}\right)\times\left(\mathbf{p}_{p,k,a}^{EN,M} - \mathbf{p}_{p,k,c}^{EN,M}\right)\right\|} \tag{22}$$

$$\mathbf{p}_{p,k}^{EN} = \mathbf{R}_{b,k}^{EN}\left(\mathbf{R}_{l}^{b}\mathbf{p}_{p,k}^{l} + \mathbf{p}_{l}^{b}\right) + \mathbf{p}_{b,k}^{EN} \tag{23}$$

where $\mathbf{p}_{p,k}^{l}$ represents the planar point in k^{th} LiDAR keyframe, $\mathbf{T}_{l}^{b} = \left[\mathbf{R}_{l}^{b}\ \mathbf{p}_{l}^{b}\right]$ denotes the transformation matrix from the LiDAR frame to the body frame, $\mathbf{T}_{b,k}^{EN} = \left[\mathbf{R}_{b,k}^{EN}\ \mathbf{p}_{b,k}^{EN}\right]$ denotes the transformation matrix from the k^{th} local body frame to the ENU frame.

GNSS observations are typically fewer than 20 in urban areas, while a 32-line mechanical LiDAR provides over 2000 observations per frame in our experiments. Integrating dense LiDAR constraints with limited GNSS observations poses two challenges. First, it increases optimization complexity, demanding more computation and reducing efficiency. Second, it disrupts the balance between GNSS and LiDAR contributions in optimization. LiDAR constraints may dominate the solution if weights account only for observation error but not quantity. Due to the high redundancy in each LiDAR frame, using fewer observations can reduce complexity and improve efficiency while maintaining state observability [42]. This paper analyzes how the number of LiDAR observations affects estimation uncertainty and determines the minimum required to maintain accuracy in real environments. We evaluate the effect of LiDAR observation quantity by constructing an information matrix and analyzing its eigenvalues [37]. Originally used to analyze constraint degeneracy in various environments, this method is adopted here to assess how constraint degeneracy varies with observation quantity. The degeneracy of LiDAR constraints is defined as [37]:

$$D = \lambda_{min} + 1 \tag{24}$$

where $\lambda_{\min}$ represents the smallest eigenvalue of information matrix $\boldsymbol{\Lambda}_l$. For the calculation of $\boldsymbol{\Lambda}_l$, we have:

$$\boldsymbol{\Lambda}_l = \boldsymbol{J}_p^{L^T}\boldsymbol{J}_p^{L} \tag{25}$$

where $\mathbf{J}_p^L$ denotes the Jacobian matrix of the residuals of LiDAR constraints with respect to the pose states. $\boldsymbol{\Lambda}_l$ captures the local curvature of the cost function defined by the LiDAR residuals, and serves as a proxy for the information gained from the LiDAR observations. The smallest eigenvalue λ_{min} of $\boldsymbol{\Lambda}_l$ reflects the weakest constrained state in the state space, i.e., the degree-of-freedom in which the LiDAR observations provide the least information. A small λ_{min} indicates a potential degeneracy in the constraint, such as when the point cloud lies on a flat or linear surface, offering little observability for a certain degree-of-freedom (e.g., translation orthogonal to the surface). This formulation allows us to quantitatively assess how the number of LiDAR observations contributes to the strength of the constraint.

The VS factor weight is determined by three aspects: LiDAR observation uncertainty, local map position uncertainty, and the LiDAR–GNSS observation ratio. LiDAR observation uncertainty is derived from geometric and appearance consistency between scan and map features [9]. Since the local map is continuously updated by recent estimates, its uncertainty increases over time without reliable GNSS input, due to the absence of a global constraint [43]. As a result, VS factor uncertainty grows with map uncertainty. To balance the influence of VS and real satellites, VS constraints are dynamically weighted based on the real-time ratio between VS and satellite observations:

$$w_t^l = \frac{n_{virtual}^l}{n_{real}^l} \tag{26}$$

where $n_{virtual}^l$ represents the constraint's number of VS, n_{real}^l represents the constraint number of real satellites. This enables real satellites to be effective even in small numbers, which is common in urban cases.

6. Marginalization Factor

To release the computational load and meanwhile maintain the impacts of the constraints from the previous information, marginalization is adopted in the sliding window optimization. We gradually marginalize the constraints from the older keyframes sliding out the window through the Schur complement [44]. The corresponding new prior factor is further added in the updated window.

Given the factors above, the optimized states and their respective covariance matrix are obtained after the tightly-coupled optimization. Knowing that the double-differenced integer ambiguities should indeed be integer values, the estimated float values of integer ambiguities can be resolved as integer values and the position results can be corrected with higher accuracy, whereas a fixed solution is reached. To solve the integer ambiguity resolution problem, the modified LAMBDA algorithm [4] is adopted for its efficiency.

III. Experimental Results

The proposed system is implemented using C++ on Robot Operation System (ROS) [45]. We use Ceres Solver [46] and GTSAM [47] for the nonlinear optimization as well as the pose graph optimization. The experimental evaluation is conducted on three challenging sequences collected in Hong Kong, namely

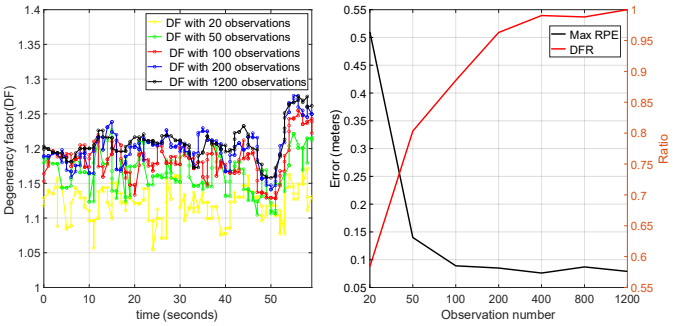

Fig. 6. Left: Degeneracy factor (DF) over time with different numbers of LiDAR observations, from 20 to 1200, shown as colored curves (yellow, green, red, blue, and black). Right: Trends of degeneracy factor ratio (DFR, red) and maximum relative positioning error (Max RPE, black) with increasing observation number.

Urban Canyon 1, Urban Canyon 2, and Urban Canyon 3, which contain various levels of urbanized scenarios. Urban Canyon 1 and 2 are collected in Kowloon Tong with duration around 150s and 400s, respectively. Urban Canyon 3 (1500s) is from our open-sourced dataset, UrbanNav [48], which is collected in Whampoa. Kowloon Tong is a medium-density urban area with relatively low-rise buildings. This region contains tree-lined streets with dense foliage, which can severely obstruct satellite signals and introduce observation errors due to NLOS or multipath effects. Whampoa is a more complex urban region with varying scenarios, including open spaces, tunnels, and areas with dense high-rise buildings. This region also features dynamic traffic such as frequent double-decker buses, which create temporary but substantial signal blockages and reflectors.

A. Experiment Platform

The data collection is based on the experimental platform proposed in UrbanNav. A low-cost GNSS receiver, the u-blox M8T, is employed to collect raw single-frequency GPS/BeiDou signals at 10 Hz. The Xsens Mti-10 IMU is adopted to collect inertial measurements at a frequency of 100 Hz. A HDL-32E LiDAR collects 3D measurements at a frequency of 10 Hz. Moreover, the NovAtel SPAN-CPT, an integration system from multi-frequency and constellation GNSS-RTK and IMU with fiber-optic gyroscopes (FOG, 1 degree per hour for gyroscope bias, 0.067 degrees per hour as random walk), is employed to provide ground truth. In the implementation, data from different sources are synchronized via Pulse-Per-Second (PPS) hardware in the computer. The extrinsic parameters between different sensors are carefully calibrated before the experiments. The initial transformation from local coordinates to global coordinates is provided in advance by aligning the first position to the ground truth.

B. Evaluation of the impact of different numbers of LiDAR observations on the degeneracy factor of state estimation

We analyze how the degeneracy factor varies with the number of LiDAR observations. Fig. 6 shows the degeneracy factor

across different observation numbers. With only 20 observations per frame, the degeneracy factor remains low, indicating insufficient constraints and high estimation uncertainty. Increasing the number of observations raises the degeneracy factor. This means that with more available observations, the state uncertainty will be significantly reduced due to stronger constraints. As shown in the right panel of Fig. 6, we use the degeneracy factor ratio (DFR) and the maximum relative positioning error (Max RPE) to show how positioning accuracy varies with observation count. The DFR is obtained by calculating the ratio of the degradation factor with a specific number of LiDAR observations and with a sufficient number of LiDAR observations (the sufficient number is set to 1200). For clarity, we compute DFR using the minimum eigenvalue of the information matrix, slightly differing from (24). The Max RPE is obtained by evaluating the relative positioning performance of the LIO system [9] with a specific number of LiDAR observations. As shown in the right panel of Fig. 6, using 20 observations results in higher LiDAR positioning errors, which can degrade final integrated positioning accuracy, and accuracy improves with more observations. We define the minimum number of observations where DFR and Max RPE curves first stabilize as the effective threshold. We can see that DFR increases and stabilizes around 0.95 once the number of features exceeds 200, while the pose error remains below 0.1m. These trends indicate that 200 observations are sufficient to capture the constraint information of all available features, offering a good trade-off between performance and computational efficiency. In this paper, we use 200 LiDAR observations per frame. The evaluation of final positioning accuracy and the system efficiency is provided in the following sections.

C. Evaluation of the performance of the 3D LiDAR aided NLOS mitigation

Unlike traditional methods, 3DLA NLOS detection does not depend on position estimation but instead relies on attitude accuracy and environmental reconstruction, particularly in the vertical direction. The proposed system improves on previous 3DLA methods by using global PGO to update the 3D PCM for NLOS detection. This addresses false NLOS detections caused by PCM drift in earlier methods [23]. Fig. 7 illustrates how attitude drift leads to incorrect NLOS classification. The left panel shows NLOS detection using the drift-free PCM; the right uses drifted PCM, whose attitude is estimated through LIO and Doppler velocity. Accumulated attitude drift distorts satellite occlusion and hinders correct NLOS detection. As shown in Table II, the drifted case results in higher positioning error due to undetected NLOS receptions and misclassified healthy measurements.

We evaluate the method using different sliding window lengths to assess how PCM reconstruction affects NLOS detection. Fig. 8 compares NLOS detection using PCMs from different window sizes. With 60 keyframes (left) and 20 keyframes (right), the upper building structure is more complete in the left case. A larger window enables more complete reconstruction and more accurate satellite occlusion detection. Table II summarizes the evaluation results.

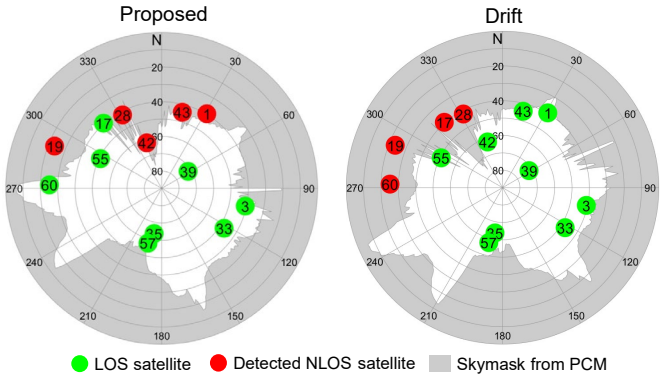

Fig. 7. Comparison between the NLOS detection methods based on the globally optimized drift-free PCM (left) and the drifted PCM (right). The skymasks generated from different PCMs are shown in gray.

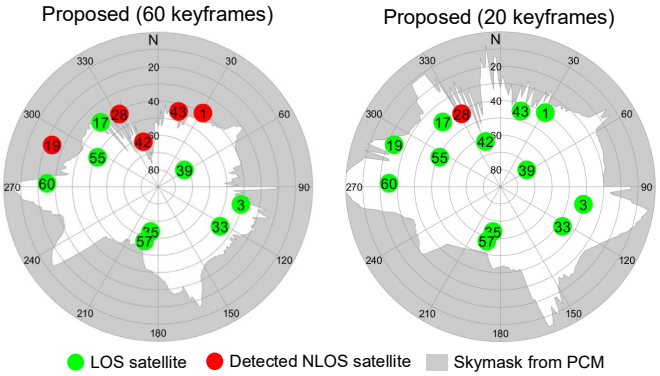

Fig. 8. Comparison between the results of NLOS detection methods based on different sliding window sizes.

To evaluate the long-term performance of the proposed 3DLA NLOS mitigation method with existing representative method, we compare it with 3DMA GNSS-RTK [16] in terms of NLOS detection, as shown in Fig. 9. Both methods are evaluated in Urban Canyon 3. We use 3D building model from the Hong Kong Common Spatial Data Infrastructure Portal for 3DMA. Both methods show similar trends, with more NLOS detections during rapid changes in satellite availability. The proposed method detects more NLOS signals on average, as it uses real-time 3D PCM that better captures signal occlusion from buildings, vehicles, vegetation, and infrastructure. In contrast, 3DMA GNSS-RTK is constrained by 3D model resolution and cannot account for dynamic or non-building occlusions. However, the proposed method's sensitivity to dynamic environments may lead to excessive NLOS exclusion, degrading satellite geometry. Therefore, in loosely-coupled systems, the proposed method can be combined with traditional residual-based outlier detection for better result when the system is initialized.

D. Evaluation of the positioning performance of the proposed tightly-coupled GNSS/LiDAR/INS integration with 3D LiDAR aided NLOS mitigation

To evaluate the positioning performance of the proposed method, the following methods are evaluated and compared

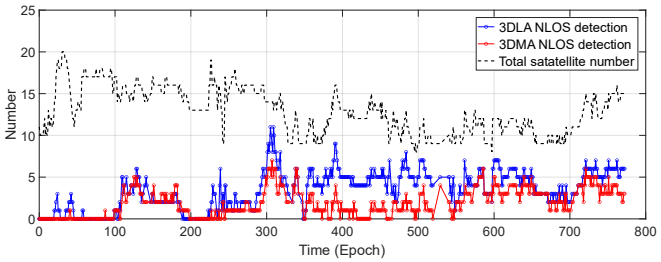

Fig. 9. NLOS detection comparison between different methods. The black dashed line represents the number of the received satellites. The red line marked with circles denotes the number of detected NLOS satellites from the 3DMA GNSS-RTK method, and the blue line marked with circles denotes the number of detected NLOS satellites from the proposed method.

TABLE II
POSITIONING PERFORMANCE (METERS) OF THE EVALUATED THREE CASES FOR THE SELECTED EPOCH IN URBAN CANYON 1.

All data	Drift PCM	Proposed (20 keyframes)	Proposed (60 keyframes)
3D Error (m)	1.96	1.17	**0.55**

qualitatively and quantitatively in multiple aspects. First, mean error, maximum error, and standard deviation in both 2D and 3D cases will demonstrate the positioning accuracy of different methods. Second, we utilize the ambiguity fixing rate to indicate the effectiveness of geometry improvement by the proposed method. The ambiguity fixing rate indicates the percentage of fixed solutions to the total number of solutions. The successfully fixed solution is determined when the 3D positioning error is less than 20cm and the ratio test is passed with threshold 3. Moreover, the availability is evaluated to compare the positioning ability, which is the percentage of the number of solutions to the total number of epochs. The evaluated methods are listed as follows:

1. **GNSS-RTK**: RTKLIB (v2.4.3) [49] is evaluated to represent the performance of conventional GNSS-RTK. Forward filtering is adopted under the fix-and-hold condition.
2. **LIO**: LiDAR/Inertial integration method [9] is evaluated to demonstrate the performance of pure LiDAR/inertial odometry.
3. **LC GNSS-RTK-LIO**: Loosely-coupled integration between GNSS-RTK and LIO system [50]. This is performed to show the improvement of positioning by loosely integrating the GNSS-RTK with the LIO system compared with standalone systems.
4. **TC GNSS-LIO**: Tightly-coupled integration system between GNSS, LiDAR, and IMU. We select the implementation in [30] due to its effectiveness and availability as open-source project. this is to show the performance of a tightly-coupled system as a baseline for evaluation.
5. **3DLA GNSS-RTK**: The proposed tightly-coupled VS-aided GNSS-RTK/IMU integrated system. This is to show the effectiveness of geometry improvement by VS.

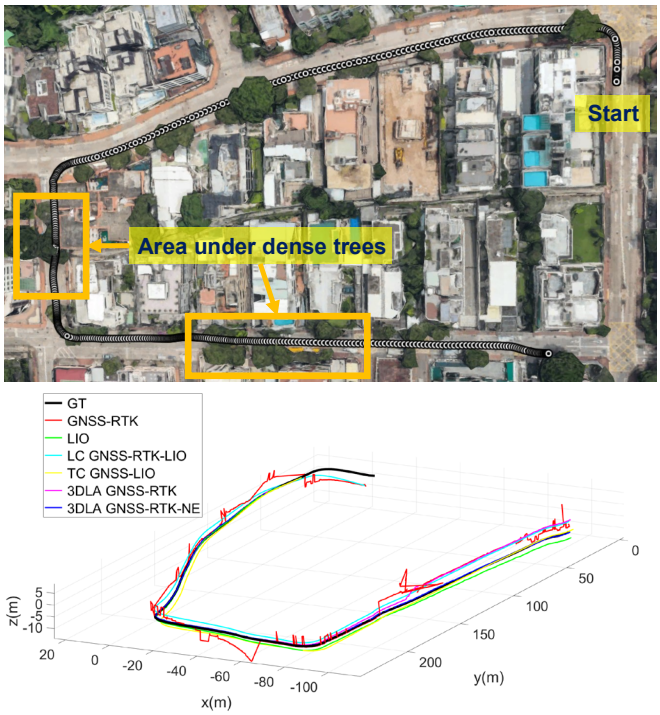

Fig. 10. The trajectory in Urban Canyon 1. The upper panel shows the projected trajectories on *Google Earth*. The orange box denotes the area with challenging signal blockage by trees. The lower panel shows the 3D trajectories of different methods. The red, green, cyan, yellow, magenta and blue curves denote GNSS-RTK, LIO, LC GNSS-RTK-LIO, TC GNSS-LIO, 3DLA GNSS-RTK, and 3DLA GNSS-RTK-NE, respectively. The black curve denotes the ground truth (GT) trajectory.

6. **3DLA GNSS-RTK-NE**: The proposed tightly-coupled VS-aided GNSS-RTK/IMU integrated system with drift-free NLOS exclusion. This is to demonstrate the final performance of the proposed method.

1. Evaluation of Urban Canyon 1

Table III shows the evaluation results of each method. The trajectory and the 3D positioning error are illustrated in Fig. 10 and Fig. 11. GNSS-RTK yields a 2D mean error of 1.55 m and a 3D mean error of 3.54 m, with maximum errors of 15.88 m (2D) and 29.23 m (3D). The large errors (orange box in Fig. 10; 70s and 120s in Fig. 11) occur in areas with dense buildings and trees, causing severe NLOS and degraded accuracy. As a result, the conventional GNSS-RTK method only achieves an ambiguity fixing rate of 1.61%. LIO method achieved a mean error of 0.32m in 2D and 1.30m in 3D. It is worth noting that the 2D accuracy of LIO was achieved in a relatively short trajectory with limited dynamic objects. In more challenging urban environments with longer trajectories and frequent dynamic interference, maintaining such accuracy becomes significantly more difficult. In vertical direction, LIO drifts over distance, reaching a maximum 3D error of 2.79 m. The loosely coupled LC GNSS-RTK-LIO shows intermediate performance between GNSS-RTK and LIO, as LIO can only help GNSS-RTK with relative pose constraints to

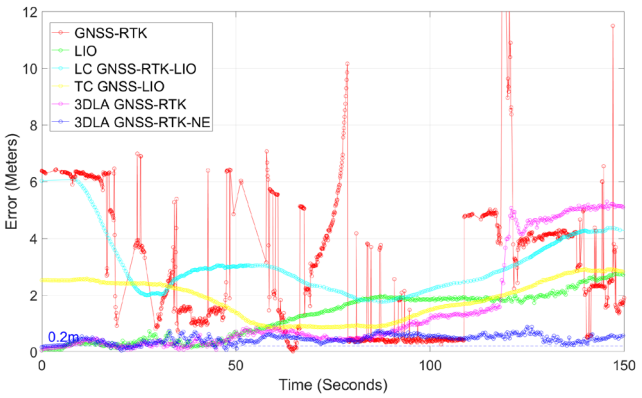

Fig. 11. 3D positioning error in Urban Canyon 1. The red, green, cyan, yellow, magenta and blue curves denote GNSS-RTK, LIO, LC GNSS-RTK-LIO, TC GNSS-LIO, 3DLA GNSS-RTK, and 3DLA GNSS-RTK-NE, respectively.

TABLE III
POSITIONING PERFORMANCE IN URBAN CANYON 1. 2D MEAN/3D MEAN REPRESENTS HORIZONTAL AND 3D POSITIONING ERRORS IN METERS. THE IMPROVEMENT (IMPR.) IS CALCULATED BASED ON THE MEAN OF GNSS-RTK. STD DENOTES THE STANDARD DEVIATION. "AVAIL." DENOTES THE AVAILABILITY.

ALL DATA	GNSS -RTK	LIO	LC GNSS -RTK-LIO	TC GNSS -LIO	3DLA GNSS -RTK	3DLA GNSS -RTK-NE
2D MEAN	1.54	**0.32**	1.42	0.86	0.39	0.36
2D MAX	18.79	0.97	3.35	2.19	0.76	**0.83**
2D STD	1.37	0.23	0.63	0.49	0.16	**0.16**
2D IMPR.	-	**79.3%**	8.39%	44.1%	74.4%	76.7%
3D MEAN	2.96	1.30	3.00	1.84	1.53	**0.44**
3D MAX	21.38	2.79	6.07	2.90	5.29	**0.87**
3D STD	2.41	0.81	0.88	0.70	1.78	**0.15**
3D IMPR.	-	63.2%	15.2%	37.9%	56.8%	**87.5%**
AMBIGUITY FIXING RATE	1.43%	-	-	-	5.98%	**11.2%**
AVAIL.	88.3%	100%	100%	100%	100%	**100%**

provide a smoother positioning result, but the global positioning accuracy is dominated by GNSS-RTK solutions. The positioning accuracy of LC GNSS-RTK-LIO is 1.42m in 2D and 3.00m in 3D with better smoothness compared with the result of GNSS-RTK. In other words, loosely-coupled integration reduces long-term drift but remains limited by GNSS-RTK accuracy. In addition, the TC GNSS-LIO method achieves 2D and 3D positioning accuracies of 0.86 m and 1.84 m, respectively. This outperforms LC systems by fully utilizing all observations and applying residual-based fault exclusion [30]. However, some positioning errors remain in certain areas. This is likely because the residual-based fault exclusion relies on the initial solution, which may not reliably identify faults in challenging urban scenarios. Moreover, the TC GNSS-LIO implementation uses only pseudorange constraints, without incorporating carrier-phase and ambiguity constraints. Therefore, the improvement is still limited by unhealthy GNSS measurements and underutilized complementary characteristics of GNSS and LiDAR/IMU.

3DLA GNSS-RTK, a tightly coupled system integrating GNSS DD pseudorange, carrier phase, Doppler, VS, and IMU, shows significant improvement compared with the conventional GNSS-RTK method and its integration with LIO: 2D error and 3D error decrease to 0.39 and 1.53m, whereas the standard deviation and maximum error are 1.78 and 5.29m respectively for the 3D case. It improves performance by fusing all raw measurements and enhancing satellite geometry through VS. The ambiguity fixing rate of 3DLA GNSS-RTK reaches 5.98%, yet the potential NLOS receptions are still not excluded. Therefore, 3DLA GNSS-RTK-NE is performed to further demonstrate the effectiveness of the proposed NLOS exclusion method. 3DLA GNSS-RTK-NE achieves the best results: 2D/3D errors of 0.36 m/0.44 m, 3D standard deviation of 0.15 m, and max error of 0.87 m. The ambiguity fixing rate of the whole trajectory by 3DLA GNSS-RTK-NE reaches 11.24%. These two observations demonstrate that the NLOS exclusion and the geometry improvement through the VS can make significant contributions to the final positioning result.

3. Evaluation of Urban Canyon 2

We further evaluate the system in Urban Canyon 2 to show its effectiveness in a more urbanized area. Table IV demonstrates the results of the compared methods, and Fig. 12 and Fig. 13 illustrate the 3D trajectory and 3D positioning errors. Urban Canyon 2 poses greater positioning challenges due to denser buildings and vegetation. GNSS-RTK achieves a 1.81m 2D mean error and a 3.65m 3D mean error. The maximum 3D error reaches 55.59m with 5.27m as the standard deviation. The overall ambiguity fixing rate is 2.86%. LIO outperforms standalone GNSS-RTK with 2D and 3D errors of 1.76 m and 1.97 m, respectively. The increasing trend of the LIO positioning error in Fig. 13 indicates the accumulated drift. Furthermore, the LC GNSS-RTK-LIO achieves 1.38m mean error in the 2D case and 2.77m in the 3D case. LC GNSS-RTK-LIO outperforms LIO because the trajectory is longer and the drift error of LIO is larger. In conclusion, the loose integration between LIO and GNSS-RTK helps to obtain a better positioning result, but the impact of the NLOS receptions and non-ideal geometry distribution are still not compensated. Tightly coupled GNSS-LiDAR integration achieves better accuracy, with 2D and 3D errors of 1.19 m and 1.96 m. However, the presence of relatively large errors suggests that residual-based fault detection is not sufficiently robust in complex urban environments. A similar limitation is observed in the proposed 3DLA GNSS-RTK method. Although the geometric distribution is improved by incorporating LiDAR observations, the positioning accuracy is still affected by NLOS receptions. The 2D mean positioning error of 3DLA GNSS-RTK is 0.61 m, with an ambiguity

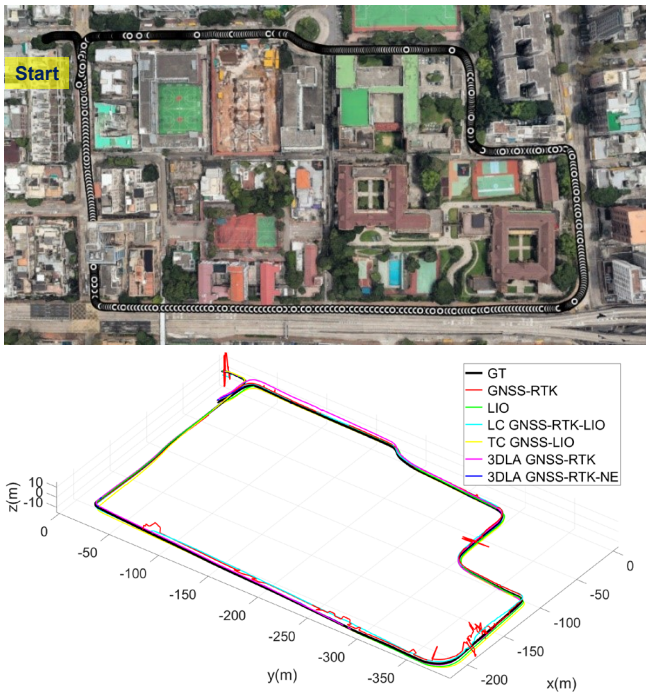

Fig. 12. The trajectory in Urban Canyon 2. The upper panel shows the projected trajectories on Google Earth. The lower panel shows the 3D trajectories of different methods. The red, green, cyan, yellow, magenta and blue curves denote GNSS-RTK, LIO, LC GNSS-RTK-LIO, TC GNSS-LIO, 3DLA GNSS-RTK, and 3DLA GNSS-RTK-NE, respectively. The black curve denotes the ground truth (GT) trajectory.

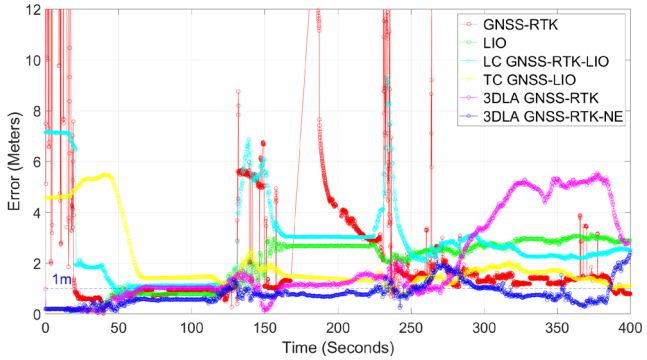

Fig. 13. 3D positioning error in Urban Canyon 2. The red, green, cyan, yellow, magenta and blue curves denote GNSS-RTK, LIO, LC GNSS-RTK-LIO, TC GNSS-LIO, 3DLA GNSS-RTK, and 3DLA GNSS-RTK-NE, respectively.

resolution rate of 5.64%. Therefore, 3DLA GNSS-RTK-NE with accurate NLOS exclusion is finally performed and achieves the best accuracy with 2D mean error and 3D mean error decreasing to 0.49m and 0.79m respectively. Meanwhile, the maximum error and the standard deviation in 2D and 3D cases are 1.44/0.22m and 2.16/0.42m. The ambiguity fixing rate of the 3DLA-NE reaches the highest level of all five methods at 7.43%. The Urban Canyon 2 results further validate the effectiveness of 3DLA NLOS exclusion and geometry improvement.

TABLE IV
POSITIONING PERFORMANCE IN URBAN CANYON 2. 2D MEAN/3D MEAN REPRESENTS HORIZONTAL AND 3D POSITIONING ERRORS IN METERS. THE IMPROVEMENT (IMPR.) IS CALCULATED CONCERNING THE MEAN OF GNSS-RTK. STD DENOTES THE STANDARD DEVIATION. "AVAIL." DENOTES THE AVAILABILITY.

ALL DATA	GNSS-RTK	LIO	LC GNSS-RTK-LIO	TC GNSS-LIO	3DLA GNSS-RTK	3DLA GNSS-RTK-NE
2D MEAN	1.81	1.76	1.38	1.19	0.61	**0.49**
2D MAX	47.28	3.15	6.74	3.08	1.54	**1.44**
2D STD	2.20	0.95	1.21	0.32	0.36	**0.22**
2D IMPR.	-	2.8%	23.75%	34.25%	68.72%	**74.87%**
3D MEAN	3.65	1.97	2.77	1.96	2.02	**0.79**
3D MAX	55.59	3.15	9.39	5.47	5.55	**2.16**
3D STD	5.27	0.97	1.58	1.21	1.70	**0.42**
3D IMPR.	-	46.%	24.11%	46.3%	44.65%	**78.36%**
AMBIGUITY FIXING RATE	2.8%	-	-	-	5.64%	**7.43%**
AVAIL.	94.%	100%	100%	100%	100%	**100%**

3. Evaluation of Urban Canyon 3

We further evaluate the system in Urban Canyon 3, a highly urbanized area. Table V presents the results of the compared methods, while Fig. 14 and Fig. 15 illustrate the 3D trajectory and 3D positioning error. The GNSS-RTK method achieves a 2D mean error of 5.11m and a 3D mean error of 9.90m. The maximum 3D error nears 100 m, with a standard deviation of 15.67 m. The overall ambiguity fixing rate is 1.22%. The LIO method shows a 2D error of 12.63 meters and a 3D error of 28.37 meters due to significant trajectory drift. LC GNSS-RTK-LIO achieves 2D and 3D errors of 2.67 m and 4.41 m, respectively, with a maximum 3D error of 16.68 m. While better than GNSS-RTK or LIO, the errors remain considerable. Tightly coupled TC GNSS-LIO further improves accuracy. The 2D positioning accuracy reaches 1.68 m, and the 3D accuracy reaches 3.34 m. However, 3DLA GNSS-RTK performs worse than TC GNSS-LIO. This is because TC GNSS-LIO reduces the impact of NLOS errors through residual-based fault exclusion. As a result, a large 3D positioning error is observed around 570s and 890s in Fig. 15, where the presence of double-decker buses and dense buildings in the surrounding area results in a significant amount of reflected signal receptions. Finally, 3DLA GNSS-RTK-NE with NLOS exclusion achieves the best accuracy: 1.02 m (2D) and 2.13 m (3D). The maximum error and standard deviation in the 2D and 3D cases are 2.57/0.52 meters and 6.27/1.50 meters, respectively. The ambiguity fixing rate of the 3DLA-NE method reaches the highest level at 8.72%. Urban Canyon 3 results underscore the importance of robust NLOS mitigation for long-term stability in dense urban areas. However, LiDAR observations often face degradation when encountering a large number of dynamic objects or traversing featureless regions. When both LiDAR and GNSS geometries are poor (e.g., at 250s and 900s), estimation accuracy inevitably degrades.

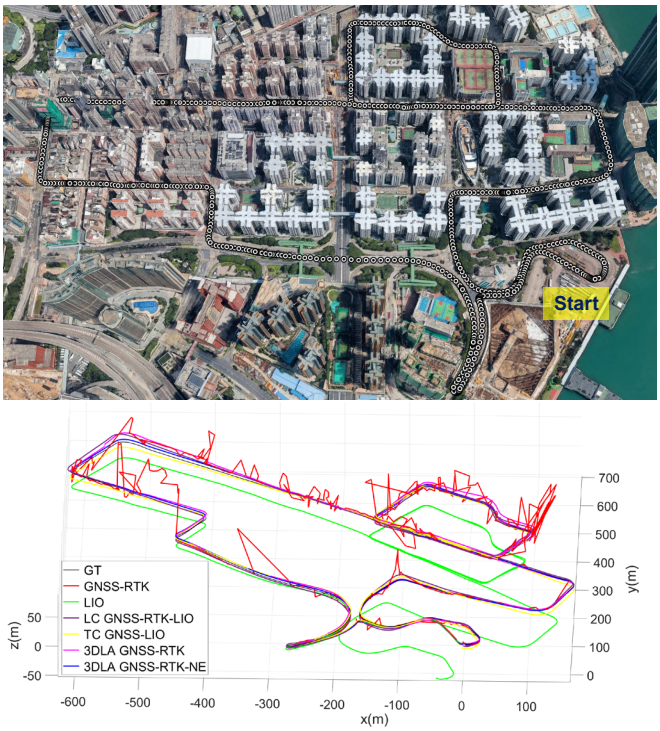

Fig. 14. The trajectory in Urban Canyon 3. The upper panel shows the projected trajectories on Google Earth. The lower panel shows the 3D trajectories of different methods. The red, green, cyan, yellow, magenta and blue curves denote GNSS-RTK, LIO, LC GNSS-RTK-LIO, TC GNSS-LIO, 3DLA GNSS-RTK, and 3DLA GNSS-RTK-NE, respectively. The black curve denotes the ground truth (GT) trajectory.

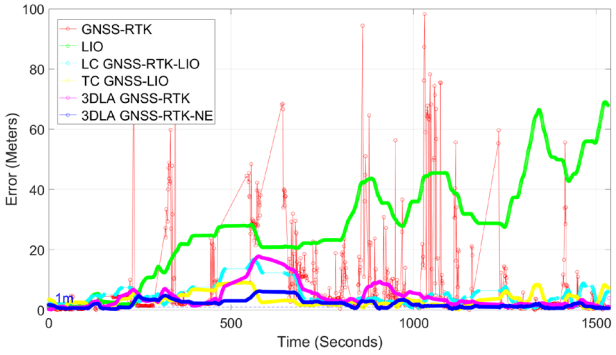

Fig. 15. 3D positioning error in Urban Canyon 3. The red, green, cyan, yellow, magenta and blue curves denote GNSS-RTK, LIO, LC GNSS-RTK-LIO, TC GNSS-LIO, 3DLA GNSS-RTK, and 3DLA GNSS-RTK-NE, respectively.

E. Evaluation of different weighting strategies for GNSS and LiDAR integration

The weight ratio design between VS and real satellites in (26) is determined based on the accuracy of the observations and their constraint characteristics. In our implementation, due to the similar absolute constraint characteristics and the significant difference in observation quantity of LiDAR and GNSS measurements, GNSS/LiDAR fusion without properly balancing their contributions to the state estimation problem may result in suboptimal performance. In this paper, we introduce a balancing weighting strategy to moderate the relative influence of each sensor's contribution. To validate its effectiveness, we conduct experiments in Urban Canyon 1, comparing performance with and without the re-weighting strategy. Following configurations are compared:

1. **3DLA GNSS-RTK without reweighting**: where no additional balancing is applied, and the optimization is directly influenced by the uncertainty and relative quantity of LiDAR and GNSS measurements.
2. **3DLA GNSS-RTK with reweighting**: where we apply the reweighting to balance the contribution from GNSS and LiDAR to the optimization.
3. **3DLA GNSS-RTK with reweighting and increased GNSS weighting (10× and 20×)**: where the weights of GNSS factor are further increased to explore whether larger GNSS weighting improves the positioning performance.

As shown in Fig. 16, directly integrating GNSS observations without reweighting improves the trajectory accuracy compared to the LIO baseline. However, since the number of reliable GNSS observations is limited during most of the sequence, the overall improvement is marginal, and the error curve remains close to that of the standalone LIO result. When the reweighting strategy is applied to balance the influence of GNSS and LiDAR observations, the positioning accuracy improves significantly. This is attributed to the increased weight of GNSS constraints, including pseudorange and carrier-phase measurements, which helps suppress the drift in LIO estimation. We further increase the GNSS weights by a factor of 10 and 20, respectively, to examine whether stronger GNSS contribution leads to better performance. The results show that while the trajectory remains stable, the

TABLE V
POSITIONING PERFORMANCE IN URBAN CANYON 3. 2D MEAN/3D MEAN REPRESENTS HORIZONTAL AND 3D POSITIONING ERRORS IN METERS. THE IMPROVEMENT (IMPR.) IS CALCULATED CONCERNING THE MEAN OF GNSS-RTK. STD DENOTES THE STANDARD DEVIATION. "AVAIL." DENOTES THE AVAILABILITY.

ALL DATA	GNSS-RTK	LIO	LC GNSS-RTK-LIO	TC GNSS-LIO	3DLA GNSS-RTK	3DLA GNSS-RTK-NE
2D MEAN	5.11	12.63	2.67	1.68	2.08	**1.02**
2D MAX	45.38	45.51	7.89	4.17	6.70	**2.57**
2D STD	7.75	12.56	1.80	0.96	1.54	**0.52**
2D IMPR.	-	-	47.75%	67.12%	59.29%	**80.04%**
3D MEAN	9.90	28.37	4.41	3.34	4.54	**2.13**
3D MAX	98.85	69.07	16.68	9.15	17.77	**6.27**
3D STD	15.67	16.94	3.34	2.21	4.09	**1.50**
3D IMPR.	-	-	55.44%	66.22%	54.14%	**78.48%**
AMBIGUITY FIXING RATE	1.2%	-	-	-	1.26%	**8.72%**
AVAIL.	60.%	100%	100%	100%	100%	**100%**

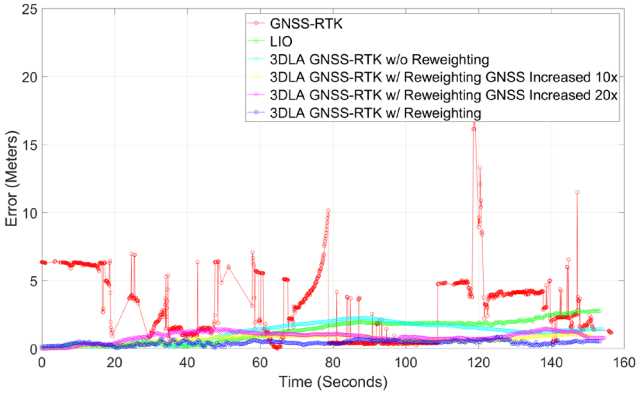

Fig 16. 3D positioning error comparison under different weighting strategies for GNSS and LiDAR integration in Urban Canyon 1. The red, green, cyan, yellow, magenta and blue curves denote GNSS-RTK, LIO, 3DLA GNSS-RTK without reweighting, 3DLA GNSS-RTK with reweighting and GNSS weight increasing (by a factor of 10 and 20), and 3DLA GNSS-RTK with reweighting, respectively.

accuracy does not improve further and, in some segments, even slightly degrades. This may be due to remained NLOS receptions, multipath effects, or cycle slips that bring local distortions to state estimation. In conclusion, improving the localization accuracy of a tightly coupled system in complex urban environments not only requires robust outlier mitigation for both LiDAR and GNSS observations, but also a well-balanced fusion strategy. In this work, the proposed reweighting formulation in (26) effectively balances the contributions from the two sensors, leading to enhanced positioning performance.

F. Evaluation of the computational efficiency of the proposed tightly-coupled GNSS/LiDAR/INS integration with 3D LiDAR aided NLOS mitigation

Computational efficiency is crucial for real-time positioning systems. The time performance of the proposed system is now analyzed. The testing device is equipped with an i9-12900K CPU and 32GB of memory, and the proposed system is operated based on a single-core, single-thread execution. It is worth mentioning that we also provide the runtime of the system based on different numbers of LiDAR observations. Fig. 17 illustrates the computational consumption, where we divide the total runtime into three parts: preprocessing, optimization, and AR. The preprocessing stage includes sensor data processing, NLOS detection, and constructing the factor graph. For different numbers of LiDAR observations, this step takes a relatively similar amount of time. It can be further observed that the optimization process consistently consumes the most time, followed by AR. Additionally, as the number of LiDAR observations increases, the time required for optimization rapidly extends. This is because multi-sensor tightly-coupled optimization is a non-convex optimization problem, and the solving efficiency is influenced by the consistency of sensor observations and the system complexity. Increasing the number of observations raises the system complexity, thereby reducing the efficiency of solving this optimization problem. The time usage of AR demonstrates a slower upward trend with more

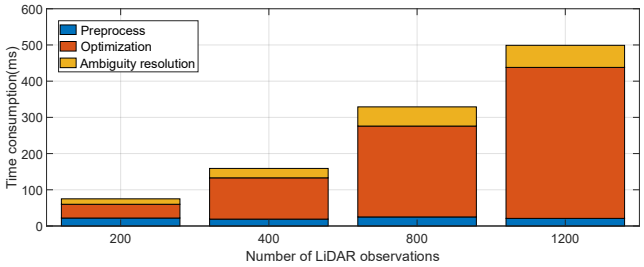

Fig. 17. Illustration of time consumption of the proposed system with different numbers of LiDAR observations. The total runtime is divided into three parts, namely preprocessing, optimization, and ambiguity resolution.

LiDAR observations, where the most time-consuming part is the estimation of the variance-covariance matrix. Different from optimization, the estimation efficiency of the variance-covariance matrix is primarily related to the state size, as the proposed system calculates it by taking the inverse of the Hessian matrix approximated by the Jacobian matrix. Computing the inverse of larger matrices requires more time. In our implementation, the sliding-window size is consistently set to 5 to ensure the efficiency of AR. Overall, using 1200 or more observations would result in a runtime exceeding 500ms, which is not applicable for real-time positioning. However, with an average runtime of around 70ms using 200 observations, it meets real-time requirements and is conducive to practical applications that require integration with other systems. Furthermore, we evaluate the runtime on a Nvidia Jetson Orin NX module, which is an edge computing unit utilizing low-power ARM processor. Under this hardware setup, the average processing time per window takes 300 milliseconds using 200 LiDAR observations, which proves that the proposed method is computationally efficient and feasible for deployment on embedded platforms.

IV. Conclusion

GNSS-RTK can provide reliable accurate positioning results in the opening areas, yet will suffer from NLOS receptions and poor satellite distribution in urban canyons. This paper presents 3DLA as 3D LiDAR-aided GNSS-RTK positioning that: (1) performs NLOS detection and exclusion based on the drift-free 3D PCM to eliminate the impact of unhealthy GNSS measurements, and (2) improves the satellite geometry distribution with great efficiency through selected low-lying VS provided by LiDAR landmarks. We evaluate the proposed system in three challenging sequences in Hong Kong. The result shows that the proposed system can achieve real-time positioning capability with higher accuracy and robustness in a highly urbanized area using commercial-level GNSS receivers and LiDAR/IMU sensor kit.

In this work, the balancing strategy between LiDAR and GNSS weights in tightly-coupled integration still needs to be improved when the local map has drifted. Our evaluations show cases where a recovery of high accuracy GNSS solutions is not immediately reflected in the integration positioning result. In future work, we will explore adaptive weighting based on online

uncertainty estimation so that reliable GNSS observations dominate more effectively, together with consistency preserving local map updates to correct drift. Moreover, the main part of the remaining positioning errors can be attributed to multipath receptions. Different from NLOS receptions, multipath receptions are more difficult to identify through LiDAR and low-cost GNSS receivers. Therefore, one possible aspect of future work can focus on the detection and correction of multipath receptions. By tackling the potential NLOS receptions first, we can refer to the residuals during the optimization to detect multipath receptions. On the other hand, the current 3DLA GNSS-RTK system is built in a sliding window optimization manner, which limits the potential of exploring the joint positioning ability of the GNSS measurements from more epochs. Given the high accuracy relative positioning ability of the LiDAR/IMU system, a method that guarantees the global consistency of both GNSS and LiDAR constraints based on a much larger sliding window would be a promising way to further enhance the positioning accuracy in a harsh urban canyon.

REFERENCES

[1] B. W. Remondi, "Performing centimeter-level surveys in seconds with GPS carrier phase: initial results," Navigation, vol. 32, no. 4, pp. 386-400, 1985.
[2] P. K. Enge, "The global positioning system: Signals, measurements, and performance," International Journal of Wireless Information Networks, vol. 1, no. 2, pp. 83-105, 1994.
[3] P. J. Teunissen, "Least-squares estimation of the integer GPS ambiguities," in Invited lecture, section IV theory and methodology, IAG general meeting, Beijing, China, 1993, pp. 1-16.
[4] X.-W. Chang, X. Yang, and T. Zhou, "MLAMBDA: A modified LAMBDA method for integer least-squares estimation," Journal of Geodesy, vol. 79, pp. 552-565, 2005.
[5] P. Xie and M. G. Petovello, "Measuring GNSS multipath distributions in urban canyon environments," IEEE Transactions on Instrumentation and Measurement, vol. 64, no. 2, pp. 366-377, 2014.
[6] W. Wen, G. Zhang, and L. T. Hsu, "Correcting NLOS by 3D LiDAR and building height to improve GNSS single point positioning," Navigation, vol. 66, no. 4, pp. 705-718, 2019.
[7] W. Wen, G. Zhang, and L.-T. Hsu, "GNSS NLOS exclusion based on dynamic object detection using LiDAR point cloud," IEEE transactions on intelligent transportation systems, vol. 22, no. 2, pp. 853-862, 2019.
[8] W. Wen and L.-T. Hsu, "3D LiDAR aided GNSS NLOS mitigation in urban canyons," IEEE Transactions on Intelligent Transportation Systems, 2022.
[9] K. Li, M. Li, and U. D. Hanebeck, "Towards high-performance solid-state-lidar-inertial odometry and mapping," IEEE Robotics and Automation Letters, vol. 6, no. 3, pp. 5167-5174, 2021.
[10] T. Shan and B. Englot, "Lego-loam: Lightweight and ground-optimized lidar odometry and mapping on variable terrain," in 2018 IEEE/RSJ International Conference on Intelligent Robots and Systems (IROS), 2018: IEEE, pp. 4758-4765.
[11] T. Qin, P. Li, and S. Shen, "Vins-mono: A robust and versatile monocular visual-inertial state estimator," IEEE Transactions on Robotics, vol. 34, no. 4, pp. 1004-1020, 2018.
[12] R. Sun, J. Wang, Q. Cheng, Y. Mao, and W. Y. Ochieng, "A new IMU-aided multiple GNSS fault detection and exclusion algorithm for integrated navigation in urban environments," GPS Solutions, vol. 25, pp. 1-17, 2021.
[13] T. Li et al., "P 3-LOAM: PPP/LiDAR loosely coupled SLAM with accurate covariance estimation and robust RAIM in urban canyon environment," IEEE Sensors Journal, vol. 21, no. 5, pp. 6660-6671, 2020.
[14] D. H. Won et al., "Selective integration of GNSS, vision sensor, and INS using weighted DOP under GNSS-challenged environments," IEEE Transactions on Instrumentation and Measurement, vol. 63, no. 9, pp. 2288-2298, 2014.
[15] G. He, X. Yuan, Y. Zhuang, and H. Hu, "An integrated GNSS/LiDAR-SLAM pose estimation framework for large-scale map building in partially GNSS-denied environments," IEEE Transactions on Instrumentation and Measurement, vol. 70, pp. 1-9, 2020.
[16] H.-F. Ng and L.-T. Hsu, "3D mapping database-aided GNSS RTK and its assessments in urban canyons," IEEE Transactions on Aerospace and Electronic Systems, vol. 57, no. 5, pp. 3150-3166, 2021.
[17] M. Adjrad, P. D. Groves, J. C. Quick, and C. Ellul, "Performance assessment of 3D - mapping - aided GNSS part 2: Environment and mapping," Navigation, vol. 66, no. 2, pp. 363-383, 2019.
[18] T. Suzuki and N. Kubo, "N-LOS GNSS signal detection using fish-eye camera for vehicle navigation in urban environments," in Proceedings of the 27th International Technical Meeting of The Satellite Division of the Institute of Navigation (ION GNSS+ 2014), 2014, pp. 1897-1906.
[19] W. Wen, X. Bai, Y.-C. Kan, and L.-T. Hsu, "Tightly coupled GNSS/INS integration via factor graph and aided by fish-eye camera," IEEE Transactions on Vehicular Technology, vol. 68, no. 11, pp. 10651-10662, 2019.
[20] W. Wen and L.-T. Hsu, "3D LiDAR aided GNSS real-time kinematic positioning," in Proceedings of the 34th International Technical Meeting of the Satellite Division of The Institute of Navigation (ION GNSS+ 2021), 2021, pp. 2212-2220.
[21] W. Wen, G. Zhang, and L.-T. Hsu, "Exclusion of GNSS NLOS receptions caused by dynamic objects in heavy traffic urban scenarios using real-time 3D point cloud: An approach without 3D maps," in 2018 IEEE/ION Position, Location and Navigation Symposium (PLANS), 2018: IEEE, pp. 158-165.
[22] W. Wen, "3D LiDAR aided GNSS and its tightly coupled integration with INS via factor graph optimization," in Proceedings of the 33rd International Technical Meeting of the Satellite Division of The Institute of Navigation (ION GNSS+ 2020), 2020, pp. 1649-1672.
[23] W. W. Wen and L.-T. Hsu, "3D LiDAR aided GNSS NLOS mitigation in urban canyons," IEEE Transactions on Intelligent Transportation Systems, vol. 23, no. 10, pp. 18224-18236, 2022.
[24] T. Hassan, T. Fath-Allah, M. Elhabiby, A. Awad, and M. El-Tokhey, "Detection of GNSS no-line of sight signals using LiDAR sensors for intelligent transportation systems," Survey Review, vol. 54, no. 385, pp. 301-309, 2022.
[25] P. Lyu, S. Bai, J. Lai, B. Wang, X. Sun, and K. Huang, "Optimal time difference-based TDCP-GPS/IMU navigation using graph optimization," IEEE Transactions on Instrumentation and Measurement, vol. 70, pp. 1-10, 2021.
[26] M. Bai, Y. Huang, Y. Zhang, and G. Jia, "A novel progressive Gaussian approximate filter for tightly coupled GNSS/INS integration," IEEE Transactions on Instrumentation and Measurement, vol. 69, no. 6, pp. 3493-3505, 2019.
[27] F. Wang and J. Geng, "GNSS PPP-RTK tightly coupled with low-cost visual-inertial odometry aiming at urban canyons," Journal of Geodesy, vol. 97, no. 7, p. 66, 2023.
[28] T. Li, H. Zhang, Z. Gao, X. Niu, and N. El-Sheimy, "Tight fusion of a monocular camera, MEMS-IMU, and single-frequency multi-GNSS RTK for precise navigation in GNSS-challenged environments," Remote Sensing, vol. 11, no. 6, p. 610, 2019.
[29] X. Wang, X. Li, H. Chang, S. Li, Z. Shen, and Y. Zhou, "GIVE: A tightly coupled RTK-inertial–visual state estimator for robust and precise positioning," IEEE Transactions on Instrumentation and Measurement, vol. 72, pp. 1-15, 2023.
[30] X. Liu, W. Wen, and L.-T. Hsu, "Glio: Tightly-coupled gnss/lidar/imu integration for continuous and drift-free state estimation of intelligent vehicles in urban areas," IEEE Transactions on Intelligent Vehicles, 2023.
[31] X. Li, H. Yu, X. Wang, S. Li, Y. Zhou, and H. Chang, "FGO-GIL: Factor graph optimization-based GNSS RTK/INS/LiDAR tightly coupled integration for precise and continuous navigation," IEEE Sensors Journal, vol. 23, no. 13, pp. 14534-14548, 2023.
[32] S. Li, S. Wang, Y. Zhou, Z. Shen, and X. Li, "Tightly Coupled Integration of GNSS, INS, and LiDAR for Vehicle Navigation in Urban Environments," IEEE Internet of Things Journal, vol. 9, no. 24, pp. 24721-24735, 2022.
[33] D. He, H. Li, and J. Yin, "LIGO: A Tightly Coupled LiDAR-Inertial-GNSS Odometry Based on a Hierarchy Fusion Framework for Global

Localization With Real-Time Mapping," IEEE Transactions on Robotics, 2025.
[34] W. Li, G. Liu, X. Cui, and M. Lu, "Feature-aided RTK/LiDAR/INS integrated positioning system with parallel filters in the ambiguity-position-joint domain for urban environments," Remote Sensing, vol. 13, no. 10, p. 2013, 2021.
[35] J. Beuchert, M. Camurri, and M. Fallon, "Factor Graph Fusion of Raw GNSS Sensing with IMU and Lidar for Precise Robot Localization without a Base Station," arXiv preprint arXiv:2209.14649, 2022.
[36] T. Li, L. Pei, Y. Xiang, X. Zuo, W. Yu, and T.-K. Truong, "P 3-LINS: Tightly Coupled PPP-GNSS/INS/LiDAR Navigation System With Effective Initialization," IEEE Transactions on Instrumentation and Measurement, vol. 72, pp. 1-13, 2023.
[37] J. Zhang, M. Kaess, and S. Singh, "On degeneracy of optimization-based state estimation problems," in 2016 IEEE International Conference on Robotics and Automation (ICRA), 2016: IEEE, pp. 809-816.
[38] C. Forster, L. Carlone, F. Dellaert, and D. Scaramuzza, "On-manifold preintegration for real-time visual--inertial odometry," IEEE Transactions on Robotics, vol. 33, no. 1, pp. 1-21, 2016.
[39] F. Huang, W. Wen, H.-F. Ng, and L.-T. Hsu, "LiDAR Aided Cycle Slip Detection for GNSS Real-time Kinematic Positioning in Urban Environments," presented at the IEEE International Intelligent Transportation Systems Conference (ITSC), 2022.
[40] J. Zhang and S. Singh, "LOAM: Lidar odometry and mapping in real-time," in Robotics: Science and systems, 2014, vol. 2, no. 9: Berkeley, CA, pp. 1-9.
[41] A. M. Herrera, H. F. Suhandri, E. Realini, M. Reguzzoni, and M. de Lacy, "goGPS: open-source MATLAB software," Gps Solut, vol. 20, no. 3, pp. 595-603, 2016.
[42] J. Jiao et al., "Greedy-based feature selection for efficient lidar slam," in 2021 IEEE International Conference on Robotics and Automation (ICRA), 2021: IEEE, pp. 5222-5228.
[43] T. Shan, B. Englot, D. Meyers, W. Wang, C. Ratti, and D. Rus, "Lio-sam: Tightly-coupled lidar inertial odometry via smoothing and mapping," in 2020 IEEE/RSJ international conference on intelligent robots and systems (IROS), 2020: IEEE, pp. 5135-5142.
[44] G. Sibley, L. Matthies, and G. Sukhatme, "Sliding window filter with application to planetary landing," J Field Robot, vol. 27, no. 5, pp. 587-608, 2010.
[45] M. Quigley et al., "ROS: an open-source Robot Operating System," in ICRA workshop on open source software, 2009, vol. 3, no. 3.2: Kobe, Japan, p. 5.
[46] S. Agarwal and K. Mierle, "Ceres solver," 2012.
[47] F. Dellaert, "Factor graphs and GTSAM: A hands-on introduction," Georgia Institute of Technology, 2012.
[48] L.-T. Hsu et al., "UrbanNav: An open-sourced multisensory dataset for benchmarking positioning algorithms designed for urban areas," in Proceedings of the 34th International Technical Meeting of the Satellite Division of The Institute of Navigation (ION GNSS+ 2021), 2021, pp. 226-256.
[49] T. Takasu and A. Yasuda, "Development of the low-cost RTK-GPS receiver with an open source program package RTKLIB," in International symposium on GPS/GNSS, 2009, vol. 1: International Convention Center Jeju Korea Seogwipo-si, Korea, pp. 1-6.
[50] J. Zhang, W. Wen, F. Huang, Y. Wang, X. Chen, and L.-T. Hsu, "GNSS-RTK Adaptively Integrated with LiDAR/IMU Odometry for Continuously Global Positioning in Urban Canyons," Applied Sciences, vol. 12, no. 10, p. 5193, 2022.

Xikun Liu received his bachelor's degree in Mechanical Design, Manufacturing, and Automation from Huazhong University of Science and Technology, China in 2017, and master's degree in Mechatronics and Information Technology from Karlsruhe Institute of Technology, Germany in 2021. He is currently a Ph.D. candidate in the Department of Aeronautical and Aviation Engineering, the Hong Kong Polytechnic University. His research interests include GNSS and sensor-aided GNSS positioning, SLAM, and multiple sensor fusion in autonomous driving.

Weisong Wen (Member, IEEE) received a BEng degree in Mechanical Engineering from Beijing Information Science and Technology University (BISTU), Beijing, China, in 2015, and an MEng degree in Mechanical Engineering from the China Agricultural University, in 2017. After that, he received a PhD degree in Mechanical Engineering from The Hong Kong Polytechnic University (PolyU), in 2020. He was also a visiting PhD student with the Faculty of Engineering, University of California, Berkeley (UC Berkeley) in 2018. Before joining PolyU as an Assistant Professor in 2023, he was a Research Assistant Professor at AAE of PolyU since 2021. He has published 30 SCI papers and 40 conference papers in the field of GNSS (ION GNSS+) and navigation for Robotic systems (IEEE ICRA, IEEE ITSC), such as autonomous driving vehicles. He won the innovation award from TechConnect 2021, the Best Presentation Award from the Institute of Navigation (ION) in 2020, and the First Prize in Hong Kong Section in Qianhai-Guangdong-Macao Youth Innovation and Entrepreneurship Competition in 2019 based on his research achievements in 3D LiDAR aided GNSS positioning for robotics navigation in urban canyons. The developed 3D LiDAR-aided GNSS positioning method has been reported by top magazines such as Inside GNSS and has attracted industry recognition with remarkable knowledge transfer.

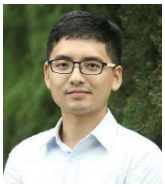

Feng Huang received his bachelor's degree from Shenzhen University in Automation in 2014 and MSc in Electronic Engineering at Hong Kong University of Science and Technology in 2016. He is a Ph.D. candidate in the Department of Aeronautical and Aviation Engineering, Hong Kong Polytechnic University. His research interests including localization and sensor fusion for autonomous driving.

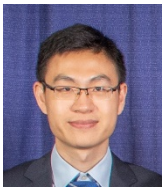

Han Gao received his Ph.D. degree from University College London (UCL) in 2019. He received a BSc degree in Aerospace Engineering from Shanghai Jiao Tong University (SJTU) in 2014. He is currently a senior software engineer at ZEEKR Technologies in China. He is interested in machine learning, localization, and mapping techniques for the autonomous system.

Yongliang Wang received the M.E. degree in the School of Electronic and Information Engineering from Xi'an Jiaotong University, China, in 2010. He is expertised in the field

of wireless signal and image processing. He is currently the chief positioning technology engineer in Riemann Lab, 2012 Laboratories, Huawei Technologies Co., Ltd.

Li-Ta Hsu received B.S. and Ph.D. degrees in aeronautics and astronautics from National Cheng Kung University, Taiwan, in 2007 and 2013, respectively. He is currently an associate professor with the Department of Aeronautical and Aviation Engineering. The Hong Kong Polytechnic University, before he served as a post-doctoral researcher at the Institute of Industrial Science at the University of Tokyo, Japan. In 2012, he was a visiting scholar at University College London, the U.K. His research interests include GNSS positioning in challenging environments and localization for pedestrians, autonomous driving vehicle, and unmanned aerial vehicle.